Andrade, J. E. *Géotechnique* [**doi:** 10.1680/geot.7.00087]

A predictive framework for liquefaction instability

J. E. ANDRADE*

A predictive framework for flow liquefaction instabilities in sands is presented. A general criterion for liquefaction, based purely on the laws of physics, is presented and adapted to the important case of radial loading (e.g. triaxial, simple shear) using the Cambridge p'–q plane. Three important contributions are made in the paper. First, the instability concept is unified, and it is shown that the liquefaction criterion coincides with other instability criteria proposed previously. Second, the mechanics triggering liquefaction instabilities are highlighted using a simple instability criterion—underscoring the role of the material state and the underlying constitutive response. Third, the proposed framework is compared with experimental data from samples of sand under undrained triaxial compression, and it is shown that the proposed criterion correctly predicts the onset of liquefaction instability as a function of the sand state. Contractive samples encounter the so-called Lade's instability line, whereas dilative samples do not liquefy, but rather undergo a phase transformation. The predictive nature of the proposed procedure may open the door to better understanding, modelling, prediction and capture of catastrophic instabilities in saturated granular materials under general loading conditions.

KEYWORDS: failure; liquefaction; numerical modelling and analysis; plasticity; sands; theoretical analysis

Cette communication présente un cadre prédictif pour les instabilités dans la liquéfaction des sables. Un critère général pour la liquéfaction, basé simplement sur les lois de la physique, est présenté et adapté au cas important des charges radiales (p. ex. cisaillement simple, triaxial) en appliquant le plan $p' - q$ de Cambridge. La présente communication apporte une contribution importante sous trois aspects ; en premier lieu, elle unifie le concept de l'instabilité, et démontre que le critère de la liquéfaction coïncide avec d'autres critères d'instabilité proposés précédemment. En deuxième lieu, elle met en vedette les aspects mécaniques déclenchant les instabilités de liquéfaction en faisant usage d'un simple critère d'instabilité, et en soulignant le rôle de l'état matériel ainsi que la réponse constitutive sous-jacente. En troisième lieu, elle compare le cadre proposé à des données expérimentales provenant d'échantillons de sable sous l'effet d'une compression triaxiale non drainée, et montre que le critère proposé permet de prédire correctement le déclenchement de l'instabilité de la liquéfaction en fonction de l'état du sable. Des échantillons à contraction prédisent la ligne d'instabilité de Lade, alors que des échantillons à dilatation ne se liquéfient pas, et subissent une transformation de phase. La nature prédictive de la procédure proposée semble mener à une optimisation de la compréhension, la modélisation, la prédiction, et la saisie des instabilités catastrophiques dans des matériaux granulaires saturés soumis à des conditions de charge générales.

INTRODUCTION

Liquefaction is one of the most devastating instabilities in saturated granular materials. In the field, it is typically associated with a build-up of pore water pressures, which in turn drive the effective mean stresses down, hence lowering the shear strength of the soil. The 1964 Niigata earthquake in Japan provided a dramatic example of the devastating effects associated with liquefaction instabilities. In this case, and others documented in history, liquefaction instabilities were responsible for slope failures, bridge and building foundation failures, and flotation of buried structures (Kramer, 1996). Even though liquefaction is usually regarded as the effect of earthquakes—and the associated cyclic loads—several researchers have shown that the intrinsic instability mechanism culprit for such unstable behaviour can occur under dynamic and static loading (Castro, 1969; Lade, 1992; Kramer, 1996; Vaid and Sivathayalan, 2000). It is now widely recognised that the unstable behaviour caused by liquefaction is associated with the so-called 'flow liquefaction' phenomenon, which occurs when the shear stress required for static equilibrium of a soil mass is greater than the shear strength of the soil in its liquefiable state (Kramer, 1996).

Manuscript received 3 May 2007; revised manuscript accepted 10 February 2009. Published online ahead of print May 2009.
Discussion on this paper is welcomed by the editor.
* Department of Civil and Environmental Engineering, Northwestern University, Evanston, USA.

The concept and definition of liquefaction are rather controversial (NRC, 1985). However, loosely defined, liquefaction can be associated with phenomena giving rise to loss of shearing resistance or to the development of excessive strains (NRC, 1985), typically accompanied by increases in pore water pressures. Liquefaction is typically divided into two main types: flow liquefaction and cyclic mobility (NRC, 1985; Kramer, 1996). The aim of this paper is to provide a simple predictive criterion to detect the onset of flow liquefaction within the framework of material instability and bifurcation analysis.

In the field, the Aberfan disaster in 1966, which claimed the lives of 144 people, 116 of them children under the age of 10, showed the world the devastating consequences of flow liquefaction. Bishop investigated the Aberfan and other instabilities of tips and spoil heaps, and contributed to setting up a framework for flow instabilities (Bishop, 1973). The framework was later refined by the US National Academy of Science's National Research Council (NRC, 1985) to define flow liquefaction as

> the condition where a soil mass can deform continuously under a shear stress less than or equal to the static stress applied to it. Equilibrium is restored, if at all, after enormous displacements or failures.

Flow liquefaction is associated with an instability that, once triggered, induces the aforementioned flow failure. Therefore flow instability is a necessary condition for flow failure, but they are not synonymous (Lade, 1999). Fig. 1 shows a

schematic of a triaxial compression test where flow liquefaction occurred, and where the difference between the instability and failure states is clearly indicated.

This paper endeavours to provide a predictive tool for the onset of flow liquefaction instability, which, as mentioned before, will lead to failure and the associated consequences of liquefaction. Furthermore, this paper frames the onset of liquefaction instability as a function of the sand state, rather than as a material parameter, such as peak shear stress, as typically assumed in practice. The importance of this fundamental difference has been pointed out by Been & Jefferies (2004), based on experimental evidence. They hypothesised that flow liquefaction could be triggered by a change in hardening modulus, rather than frictional properties (Been & Jefferies, 2004). In the present paper, liquefaction instability is associated with a limiting hardening module H_L. It is shown that the instability induces a limiting shear stress and not the other way around.

Experimentally, liquefaction flow has been studied since the 1970s. The work of Castro (1969) showed how loose specimens of sand loaded under undrained triaxial compression undergo a peak in stress space followed by a sudden 'collapse', accompanied by large pore water pressure build-up, very large deformations and profound strain-softening. On the other hand, denser samples displayed a reversal from contractive behaviour to dilative behaviour—a phenomenon that Ishihara *et al.* (1975) termed 'phase transformation'. Subsequently, Vaid & Chern (1983) performed experiments on Ottawa sand under both static and cyclic undrained triaxial loading in order to understand the effect of static shear on the resistance to liquefaction. From their experiments, they concluded that there seemed to exist a limiting effective stress ratio η_L, which controls the onset of flow deformation in loose samples (under both static and dynamic loading). This line in p'–q space has been termed the 'flow liquefaction line' (Kramer, 1996; Lade, 1999).

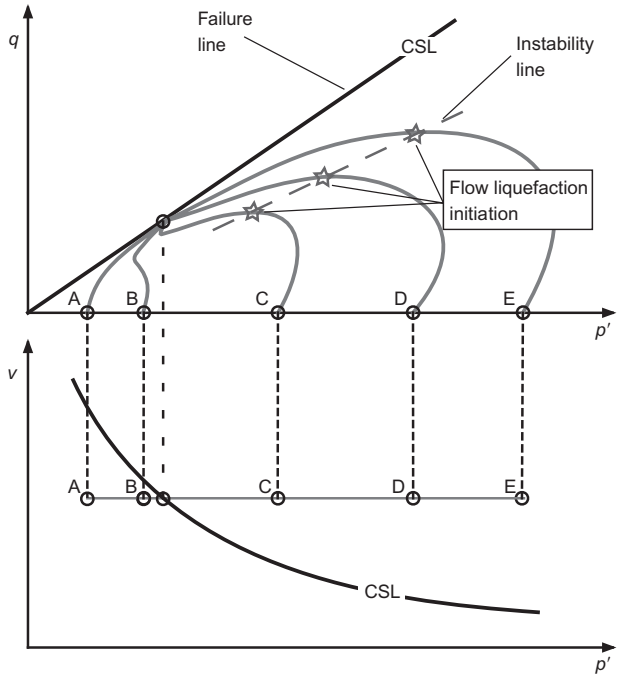

Fig. 1. Response of five specimens isotropically consolidated to the same specific volume at different effective confining pressures. Samples C, D and E undergo flow liquefaction, and the onset of instability delimits the so-called flow instability line. All five samples eventually reach the failure line, which is different than the instability line. After Kramer (1996), Lade (1999) and NRC (1985)

Motivated by the importance and catastrophic consequences of flow liquefaction, Lade & Pradel (1990) and Pradel & Lade (1990) investigated the instability and plastic flow of soils from an experimental and theoretical standpoint. The idea was to investigate the possibility of instabilities in undrained contractive sands under triaxial compression. With this objective, they used Hill's (1958) instability condition to explain the experimental observations, and concluded that fully saturated contractive samples could undergo loss of stability followed by a rapid increase in shear strains and uncontrolled pore pressure development. Pradel & Lade showed that the instability occurs below the failure line when certain kinematic conditions are present. Subsequent work by Lade (1992) postulated the formal existence of an instability line that did not coincide with failure but signalled the onset of potentially unstable states of stress. Lade showed the importance of predicting instability due to flow liquefaction in loose saturated submarine slopes as an example of the potential consequences associated with liquefaction instability.

In an effort to predict the onset of flow liquefaction and the associated deformations, several constitutive models have been proposed. Some of the most salient examples are found in the works of Lade (1992), Anandarajah (1994), Dubujet & Doanh (1997), Manzari & Dafalias (1997), Imposimato & Nova (1998a, 1998b), Wang *et al.* (2002) and Mroz *et al.* (2003). In these works, the common denominator was the application of plasticity theory, and in some cases the use of Hill's instability criterion, to identify the onset of static liquefaction.

In this paper a simple condition is proposed to detect the onset of liquefaction instability based on the laws of physics for solid–fluid mixtures (Atkin & Craine, 1976; Bowen, 1976). Furthermore, it is shown that the condition is only as predictive as the underlying constitutive model for sand. This paper does not present a constitutive model for liquefaction instability; rather, the constitutive model is general, and it is utilised to make predictions based on the liquefaction instability criterion. Direct comparisons with experimental data demonstrate the predicted ability of the framework to detect the onset of liquefaction instability. An important contribution of the paper is to demonstrate that all liquefaction criteria proposed so far collapse to one and the same, at least for the case of triaxial loading. More importantly, it is shown that there is a unified liquefaction criterion, and that the same type of analysis as followed for strain localisation (e.g. Andrade & Borja, 2006; Andrade *et al.*, 2008) can be invoked for contractive sands. This then provides a unified framework to address soil instability—a crucial step in modelling catastrophic failure. One key ingredient of this paper is a comparison of the theoretical developments with experimental results obtained by other researchers in the past. The issue of predicting and modelling soil instability, and perhaps more importantly the ensuing unbounded deformations, is of central practical importance, as exemplified by well-known geotechnical failures, such as that of the Lower San Fernando dam in southern California (Seed *et al.*, 1971). It is shown that flow liquefaction is a function of the state by way of the plastic hardening modulus.

The paper is organised as follows. The next section presents the balance equations for conservation of mass and linear momentum in a soil–fluid mixture. Following this, bifurcation analyses are performed to find the conditions for loss of uniqueness under undrained loading for a general elasto-plastic soil model. A simple liquefaction instability condition is derived in this section. In the subsequent section a particular model based on critical-state soil mechanics (CSSM) is presented. This model has been introduced before in the context of strain localisation, but it is equally capable

of modelling the behaviour of relatively loose sands. After this, the theoretical developments are compared with experimental results obtained by other researchers. In particular, two independent and complementary sets of data are used to evaluate the predictive qualities of the theory. It is shown that some of the most salient features of contractive soil behaviour observed in the laboratory are captured by the model. Some conclusions and further directions are outlined in the final section.

As for notations and symbols used in this paper, boldfaced letters denote tensors and vectors; the symbol '·' denotes an inner product of two vectors (e.g. $\boldsymbol{a} \cdot \boldsymbol{b} = a_i b_i$), or a single contraction of adjacent indices of two tensors (e.g. $\boldsymbol{c} \cdot \boldsymbol{d} = c_{ij} d_{jk}$); and the symbol ':' denotes an inner product of two second-order tensors (e.g. $\boldsymbol{c} : \boldsymbol{d} = c_{ij} d_{ij}$), or a double contraction of adjacent indices of tensors of rank two and higher (e.g. $\boldsymbol{C} : \boldsymbol{\varepsilon}^{\mathrm{e}} = C_{ijkl} \varepsilon^{\mathrm{e}}_{kl}$).

BALANCE LAWS

The balance of mass for the solid–fluid mixture reads (Andrade & Borja, 2007)

$$\nabla \cdot \boldsymbol{v} = \nabla \cdot \boldsymbol{q} \tag{1}$$

where $\boldsymbol{v}$ is the velocity of the solid and $\boldsymbol{q}$ is the relative flow vector, defined by Darcy's law for an isotropic medium. The operator ∇ is the gradient operator and $\nabla\cdot$ is the divergence operator. Similarly, the balance of linear momentum (equilibrium) equation for the solid–fluid system under quasi-static conditions reads (Andrade & Borja, 2007)

$$\nabla \cdot \boldsymbol{\sigma} + \rho \boldsymbol{g} = \boldsymbol{0} \tag{2}$$

where $\boldsymbol{\sigma}$ is the total stress tensor, ρ is the density of the mixture and $\boldsymbol{g}$ is the gravitational acceleration vector. Following Terzaghi's decomposition of the total stress tensor, the effective stress tensor is defined as

$$\boldsymbol{\sigma}' = \boldsymbol{\sigma} - p\boldsymbol{1} \tag{3}$$

where the geomechanics convention is used with compressive stresses and strains being positive, and the pore pressure p always being positive in compression. The tensor $\boldsymbol{1}$ is the identity matrix.

LIQUEFACTION CRITERIA

Recently, Borja (2006) derived a general criterion for liquefaction based on isotropic elasto-plasticity and the balance laws presented above. Here, a liquefaction criterion is derived using slightly more simplified standard assumptions (i.e. infinitesimal deformations, two-invariant plasticity, and incompressible fluids and solids). Without loss of generality, attention is restricted to isotropic two-invariant elasto-plasticity models. Consider the classical effective stress invariants

$$p' = tr\boldsymbol{\sigma}'; \qquad q = \sqrt{\frac{2}{3}} \|\boldsymbol{\xi}'\| \tag{4}$$

where $\boldsymbol{\xi}' = \boldsymbol{\sigma}' - p'\boldsymbol{1}$ is the deviatoric component of the effective stress tensor. Hence the yield surface $F = F(p', q, \pi_{\mathrm{i}})$ and plastic potential $Q = Q(p', q, \overline{\pi}_{\mathrm{i}})$ can each be expressed as an isotropic function of the two effective stress invariants. The variables π_{i} and $\overline{\pi}_{\mathrm{i}}$ control the size of the yield surface and plastic potential respectively. As with all elasto-plastic models under infinitesimal conditions, the strain rate tensor is additively decomposed into elastic and plastic parts, such that $\dot{\boldsymbol{\varepsilon}} = \dot{\boldsymbol{\varepsilon}}^{\mathrm{e}} + \dot{\boldsymbol{\varepsilon}}^{\mathrm{p}}$. The plastic strain rates are given by the non-associative flow rule, as usual.

Loss of uniqueness in the infinitesimal case can be expressed as (Hill, 1958; Borja, 2002)

$$[[\dot{\boldsymbol{\sigma}}]] : [[\dot{\boldsymbol{\varepsilon}}]] = 0 \tag{5}$$

where $[[\dot{\boldsymbol{\varepsilon}}]] = \dot{\boldsymbol{\varepsilon}}^{*} - \dot{\boldsymbol{\varepsilon}}$ is the jump in strain rate due to potentially duplicate solutions $(\boldsymbol{v}^{*}, \boldsymbol{v})$ for the velocity field. This is the onset of bifurcation into a multiplicity of solutions. At this point, instabilities in the form of a deformation band or, in the present case of interest, liquefaction can occur. The only difference lies in the kinematics encoded in the strain rate jump $[[\dot{\boldsymbol{\varepsilon}}]]$. In the case of liquefaction, the jump in the flow vector $\boldsymbol{q}$ is forced to vanish, that is, $[[\boldsymbol{q}]] = \boldsymbol{0}$, and this condition is called undrained bifurcation. Note that undrained bifurcation is not equivalent to locally undrained conditions, that is, $\boldsymbol{q} = \boldsymbol{0}$. In any case, the balance of mass equation (1) requires

$$\nabla \cdot [[\boldsymbol{v}]] = tr[[\dot{\boldsymbol{\varepsilon}}]] = 0 \tag{6}$$

which signifies an incompressible bifurcation. At this point, the onset of liquefaction (or undrained bifurcation) is given by equation (5), conditioned to equation (6).

Within the framework of elasto-plasticity, the effective stress tensor rate takes the form

$$\dot{\boldsymbol{\sigma}}' = \boldsymbol{c}^{\mathrm{ep}} : \dot{\boldsymbol{\varepsilon}} \tag{7}$$

where $\boldsymbol{c}^{\mathrm{ep}}$ is the canonical elasto-plastic operator for all isotropic rate-independent plasticity models. Rewriting equation (5) gives $[[\dot{\boldsymbol{\varepsilon}}]] : \boldsymbol{c}^{\mathrm{ep}} : [[\dot{\boldsymbol{\varepsilon}}]] + [[\dot{p}]]\boldsymbol{1} : [[\dot{\boldsymbol{\varepsilon}}]]$, where equations (3), (5) and (7) have been used. Using the constraint of incompressible bifurcation an expression is obtained for the limiting hardening modulus under radial loading

$$H_{\mathrm{L}} = -K \partial_{p'} F \partial_{p'} Q \tag{8}$$

where K is the elastic bulk modulus. Hence when the hardening modulus is equal to the limiting hardening modulus—that is, $H = H_{\mathrm{L}}$—liquefaction instability will occur. The above condition signifies the loss of pointwise stability of the elasto-plastic operator (cf. Marsden & Hughes, 1983), something that must also happen in deformation banding bifurcations. However, the undrained bifurcation kinematics plus the contractive behaviour of the material define the liquefaction condition.

It is worth noting that H_{L} plays a similar role to the critical hardening modulus derived by Rudnicki & Rice (1975) for the case of shear band bifurcations. Also, H_{L} is not novel, in the sense that Dubujet & Doanh (1997) derived a similar expression 10 years ago based on Hill's instability criterion (Hill, 1958) without taking into account the presence of the fluid, but rather imposing incompressibility conditions. On the other hand, Borja (2006) derived a general liquefaction criterion based on the determinant of what will be referred to as the liquefaction matrix $\boldsymbol{L}$. When the determinant of the liquefaction matrix vanishes, liquefaction is attained. For the special case of incompressible constituents, small deformations and axisymmetric conditions, $\det\boldsymbol{L} = c^{\mathrm{ep}}_{\mathrm{aa}} + c^{\mathrm{ep}}_{\mathrm{rr}} - c^{\mathrm{ep}}_{\mathrm{ra}} - c^{\mathrm{ep}}_{\mathrm{ar}} = 0$ is the condition for liquefaction. Here the subscripts 'a' and 'r ' stand for axial and radial principal directions. A few lines of derivation can show that $\det\boldsymbol{L} = 0$ coincides with the condition $H = H_{\mathrm{L}}$, as shown above.

Remark 1. It is illuminating to look at the liquefaction phenomenon from the point of view of loss of controllability as defined by Nova (1994). In this context, think of a classical triaxial experiment conducted under undrained conditions. Under these conditions, one can show that the above class of elasto-plastic models boils down to

$$\begin{Bmatrix} \dot{\varepsilon}_v \\ \dot{\varepsilon}_s \end{Bmatrix} = \begin{bmatrix} \frac{1}{K} + \frac{1}{H\partial_{p'}Q\partial_{p'}F} & \frac{1}{H\partial_{p'}Q\partial_q F} \\ \frac{1}{H\partial_q Q\partial_{p'}F} & \frac{1}{3\mu} + \frac{1}{H\partial_q Q\partial_q F} \end{bmatrix} \begin{Bmatrix} \dot{p}' \\ \dot{q} \end{Bmatrix} \tag{9}$$

with μ as the elastic shear modulus, $\dot{\varepsilon}_v = \dot{\varepsilon}_a + 2\dot{\varepsilon}_r$ as the volumetric invariant and $\dot{\varepsilon}_s = \frac{2}{3}|\dot{\varepsilon}_a - \dot{\varepsilon}_r|$ as the deviatoric invariant of the strain rate tensor. Also, $\dot{p}' = \frac{1}{3}(\dot{\sigma}_a + 2\dot{\sigma}_r)$ and $\dot{q} = |\dot{\sigma}_a - \dot{\sigma}_r|$ under triaxial loading. Since liquefaction instability is associated with the peak of the p'–q stress path in an undrained triaxial test, it is required that $\dot{q} = 0$. Furthermore, under undrained conditions, $\dot{\varepsilon}_v = 0$: thus

$$\left(\frac{1}{K} + \frac{1}{H}\frac{\partial Q}{\partial p'}\frac{\partial F}{\partial p'}\right)\dot{p}' = 0 \tag{10}$$

and since $\dot{p}' \neq 0$, in general, the term inside the parentheses must vanish. It is worthwhile noting that this expression was also obtained by Pradel & Lade (1990) in the context of Hill's instability condition (see Hill, 1958). This critical term sheds some light on the mechanisms governing liquefaction instability. Consider the simplified case of associative plasticity, $F = Q$. In frictional materials, the term $\partial F/\partial p'$ is associated with the plastic volumetric strain rates, with the vanishing of such a term signifying zero volumetric plastic strain change or simple shear deformations. Elastic incompressibility would force liquefaction to occur at zero plastic volumetric strain rates. At the other extreme, large elastic compressibility would require large contractancy and/or a nearly perfectly plastic (though negative) hardening modulus. However, the elastic compressibility is usually finite (albeit small). and hence liquefaction occurs under compactive strains associated with softening. Once the material undergoes a so-called 'phase transformation point' (Ishihara *et al.*, 1975), transitioning from compaction to dilation, liquefaction cannot occur, as the material must undergo hardening to accommodate phase transformations.

CONSTITUTIVE MODEL FOR SANDS

It is clear that the liquefaction predictions are only as good as the constitutive model used. Therefore in this section a constitutive model is presented for sands that is capable of predicting the material behaviour accurately. The model is a descendant of Jefferies' Nor-Sand model (Jefferies, 1993), and it is based on CSSM. The most important features of the elasto-plastic model are presented here. The interested reader is referred to Andrade & Borja (2006) and Borja & Andrade (2006) for a detailed account of the three-invariant plasticity model in small strains and finite deformation regime, as well as numerical implementation in a non-linear finite element program. The predictive capabilities of the model under drained and undrained conditions, and for a variety of stress paths, have been outlined in a number of publications (Andrade & Borja, 2006, 2007; Borja & Andrade, 2006; Andrade *et al.*, 2008; Andrade & Ellison, 2008). The purpose of this section is briefly to describe the model for completeness of presentation.

The elastic model used herein produces pressure-dependent elastic bulk and shear moduli derived from hyperelasticity and used in Houlsby (1985), Borja *et al.* (1997) and Borja & Tamagnini (1998) for modelling granular bodies. The pressure-dependent bulk modulus takes the form

$$K = \frac{p'}{\tilde{\kappa}} \tag{11}$$

where $\tilde{\kappa}$ is the elastic compressibility of the material. By the same token, the elastic region is enclosed by the two-invariant yield surface

$$F(p', q, \pi_i) = q - p'\eta(p', \pi_i) \tag{12}$$

where

$$\eta = \begin{cases} M[1 + \ln(\pi_i/p')] & \text{if } N = 0 \\ M/N\left[1 - (1-N)(p'/\pi_i)^{N/(1-N)}\right] & \text{if } N > 0 \end{cases} \tag{13}$$

The image stress $\pi_i > 0$ controls the size of the yield surface; it is defined such that the stress ratio $\eta = q/p' = M$ when $p' = \pi_i$. The parameter $N \geqslant 0$ determines the curvature of the yield surface on a meridian plane, and it typically has a value less than or equal to 0·4 for sands (Jefferies, 1993).

Similar to the isotropic yield surface, the plastic potential is given by

$$Q(p', q, \overline{\pi}_i) = q - p'\overline{\eta}(p', \overline{\pi}_i) \tag{14}$$

where

$$\overline{\eta} = \begin{cases} M[1 + \ln(\overline{\pi}_i/p')] & \text{if } \overline{N} = 0 \\ M/\overline{N}\left[1 - (1-\overline{N})(p'/\overline{\pi}_i)^{\overline{N}/(1-\overline{N})}\right] & \text{if } \overline{N} > 0 \end{cases} \tag{15}$$

Plastic flow is associated if $\overline{N} = N$ and $\overline{\pi}_i = \pi_i$, and non-associated otherwise. It has been shown that for thermodynamic considerations $\overline{N} \leqslant N$ (Borja & Andrade, 2006), resulting in a plastic potential that is 'flatter' than the yield surface and hence in less dilatancy than under associated flow. The variable $\overline{\pi}_i$ is a free parameter that determines the final size of the plastic potential function.

State parameter, plastic dilatancy and hardening law

As mentioned earlier, the model is based on CSSM (Schofield & Wroth, 1968). In these classical models, the image stress π_i coincides with the critical state or the critical-state line (CSL). The CSL is given by the equations

$$\begin{aligned} q_c &= Mp'_c \\ v_c &= v_{c0} - \tilde{\lambda}\ln(p'_c) \end{aligned} \tag{16}$$

where the subscript 'c' denotes that the point (v_c, p'_c, q_c) is on the CSL. The material parameters are the plastic compressibility index $\tilde{\lambda}$ and the reference specific volume v_{c0}. In classic models, such as Cam-clay (Roscoe & Burland, 1968; Schofield & Wroth, 1968), undrained plastic flow can occur only on the CSL.

To apply the model to sands, which exhibit different types of volumetric yielding depending on initial density, the yield surface is detached from the critical state line along the v-axis. Thus the state point (v, p', q) may now lie either above or below the critical specific volume v_c at the same stress p', depending on whether the sand is looser or denser than critical. Following the notations of Jefferies (1993), a state parameter ψ is introduced to denote the relative distance along the v-axis of the current state point to a point v_c on the CSL at the same p'

$$\psi = v - v_c \tag{17}$$

Further, a state parameter ψ_i is introduced, denoting the distance of the same current state point to $v_{c,i}$ on the CSL at $p' = \pi_i$. The relation between ψ and ψ_i is

$$\psi_i = \psi + \tilde{\lambda}\ln\left(\frac{\pi_i}{p'}\right) \tag{18}$$

Hence ψ is negative below the CSL and positive above it. An upshot of disconnecting the yield surface from the CSL is that it is no longer possible to locate a state point on the yield surface by prescribing p' and q alone; one also needs to specify the state parameter ψ to describe the state of a point completely. Furthermore, constant-volume plastic flow does not occur only on the CSL any more, but could also take place at the image stress point. Finally, the parameter ψ_i dictates the amount of plastic dilatancy in the case of dense sands.

Formally, plastic dilatancy is defined by the expression

$$D := \dot{\varepsilon}_v^p / \dot{\varepsilon}_s^p = \frac{M - \eta}{1 - \overline{N}} \tag{19}$$

where $\dot{\varepsilon}_v^p$ and $\dot{\varepsilon}_s^p$ are the volumetric and deviatoric invariants of the plastic strain rate respectively. This definition is valid for all possible values of η, even for $\eta = 0$ where Q is not a smooth function. However, experimental evidence on a variety of sands suggests that there exists a maximum possible plastic dilatancy D^* that limits a plastic hardening response. The value of D^* depends on the state parameter ψ_i, increasing in value as the state point lies farther and farther away from the CSL on the dense side. An empirical correlation has been established experimentally in Jefferies (1993) between the plastic dilatancy D^* and the state parameter ψ_i, and takes the form $D^* = \alpha\psi_i$, where $\alpha \approx 3{\cdot}5$ typically for most sands. The corresponding size of the yield surface is

$$\frac{\pi_i^*}{p'} = \begin{cases} \exp\left(-\overline{\alpha}\psi_i / M\right) & \text{if } \overline{N} = N = 0 \\ \left(1 + \overline{\alpha}\psi_i N / M\right)^{(N-1)/N} & \text{if } 0 \leqslant \overline{N} \leqslant N \neq 0 \end{cases} \tag{20}$$

where

$$\begin{aligned} \overline{\alpha}\beta &= \alpha \\ \beta &= \frac{1 - N}{1 - \overline{N}} \end{aligned} \tag{21}$$

In the above expression a non-associativity parameter $\beta \leqslant 1$ has been introduced, where $\beta = 1$ in the associative case.

For elasto-plastic response, the standard consistency condition on the yield function results in a plastic modulus given by the equation

$$H = Mh\left(\frac{p'}{\pi_i}\right)^{1/(1-N)}\left(\pi_i^* - \pi_i\right) \tag{22}$$

where h is a hardening material constant. Since $p'/\pi_i > 0$, the sign of the plastic modulus depends on the sign of $\dot{\pi}_i$: $H > 0$ if $\dot{\pi}_i > 0$ (hardening); $H < 0$ if $\dot{\pi}_i < 0$ (softening); and $H = 0$ if $\dot{\pi}_i = 0$ (perfect plasticity). In classical Cam-clay theory the sign of H depends on the sign of $\dot{\varepsilon}_v^p$: that is, H is positive for compaction and negative for expansion. However, as noted above, this simple criterion does not adequately capture the hardening/softening responses of sands, which are shown to be dependent on the limit hardening plastic dilatancy D^*: that is, H is positive if $D > D^*$ and negative if $D < D^*$.

MODEL PREDICTIONS

The liquefaction criteria, and in particular the expression for H_L signalling the onset of liquefaction, are tested in this section against the backdrop of experimental results conducted on sands under undrained triaxial compression. It is emphasised that this section tests the predictive capabilities of the framework: it tests the ability of the simple liquefaction criterion derived earlier to detect the onset of instability, and the ability of the constitutive model presented above to capture the material behaviour. These two ingredients go together in the ensuing analyses. This section is not aimed at showing the predictive capabilities of the constitutive model, which have been demonstrated elsewhere (e.g. Andrade & Ellison, 2008).

To evaluate the predictive ability of the framework, two sets of experiments are arbitrarily selected: one conducted at constant initial void ratio while varying the confining pressure, and the other conducted at fixed confinement but different relative density. Both sets of experiments are performed under undrained triaxial compression. The initial conditions and loading paths are shown in Figs 2 and 3. These complementary sets of data provide a good test bed under the broad assumption that the samples behave homogeneously or as an element. In each case the material model presented above has been calibrated using one experimental result and then utilised to perform predictions by 'fixing' the relevant parameters.

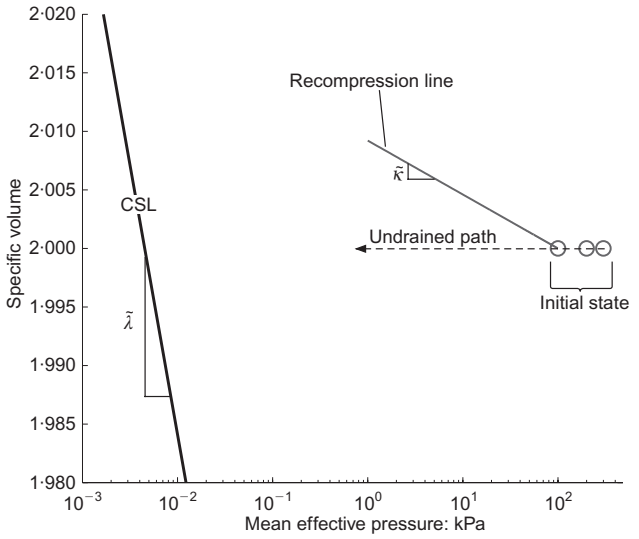

Fig. 2. Initial state and loading paths for Doanh *et al.* (1997) undrained triaxial compression experiments at various confining pressures and constant void ratio

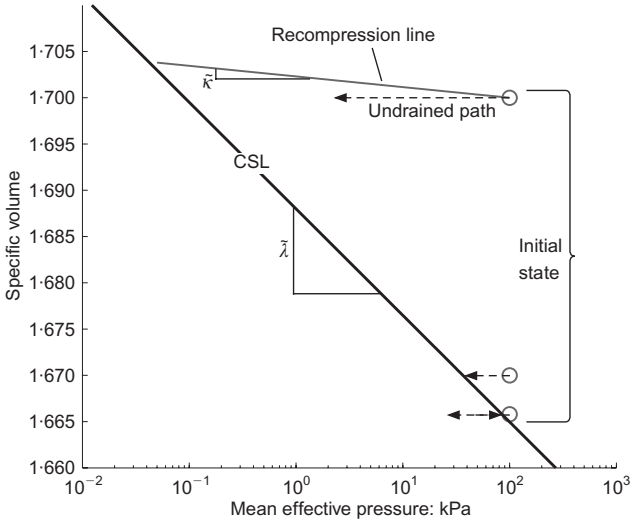

Fig. 3. Initial state and loading paths for Vaid & Chern (1983) undrained triaxial compression experiments at various relative densities and constant confining pressure

Doanh et al. (1997) experiments: constant void ratio

The first dataset is obtained from experiments conducted by Doanh *et al.* (1997) with the objective of studying static liquefaction in very loose Hostun sand under undrained triaxial compression. Comparisons are made against three experiments conducted at three different isotropic consolidation pressures: 100, 200 and 300 kPa. The three samples were prepared such that they would have the 'same' initial relative density with initial void ratios of 1·0 (see Fig. 2). The material parameters used to describe these experiments using the constitutive model presented herein are given in Table 1. These parameters are obtained by calibrating the model to match the experimental results for the undrained triaxial compression test at 100 kPa consolidation pressure. Subsequently, the parameters are kept fixed and true predictions are made for the samples failed under 200 and 300 kPa consolidation. Results of the simulations for what will be referred to as the Doanh *et al.* dataset are presented in Figs 4–6.

Figure 4 shows the stress paths for all three undrained triaxial compression experiments. Several observations can be made based on these results. First, from a constitutive modelling point of view, the model is shown to capture the material response quite well for all three stress paths. Even though the stress path for the experiment with consolidation pressure 100 kPa was used to calibrate the model, the other two stress paths are true predictions, and all three model responses capture the experimental results well. Second, and related to the first point, liquefaction instability predictions are made based on the liquefaction criterion outlined in equation (8). Clearly, success of the liquefaction criterion is highly dependent on the success of the constitutive response. To illustrate this point, Fig. 5 shows the evolution of the hardening modulus H and the limiting hardening modulus H_L as a function of pressure for the simulation at consolidation pressure 100 kPa. As explained in earlier, liquefaction occurs when $H = H_L$, marked by the 'star' symbols in Figs 4 and 5. Similar analyses were performed for the 200 kPa

Table 1. Summary of material parameters for Doanh *et al.* experiments dataset

Parameter	Value
Elastic compressibility, $\tilde{\kappa}$	0·002
Shear modulus, μ: kPa	40 000
Plastic compressibility, $\tilde{\lambda}$	0·02
Critical state parameter, M	1·0
Reference specific volume, v_{c0}	1·892
Yield function, N	0·1
For plastic potential, $\overline{N}$	0·1
Hardening coefficient, h	330

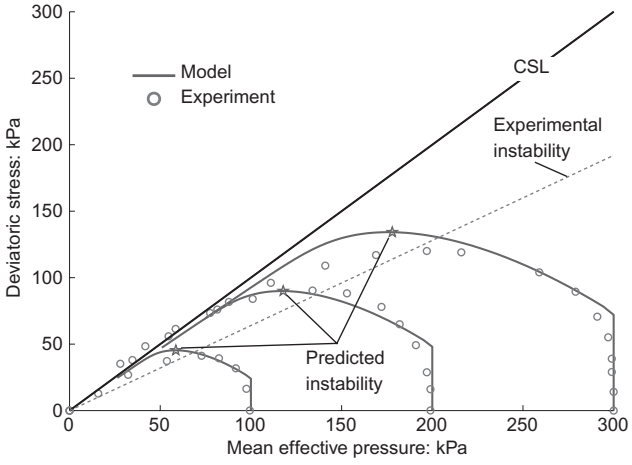

Fig. 4. Predicted stress paths and onset of liquefaction instability compared with results obtained by Doanh *et al.* (1997) from undrained triaxial compression experiments in very loose sands at various confining pressures and constant void ratio

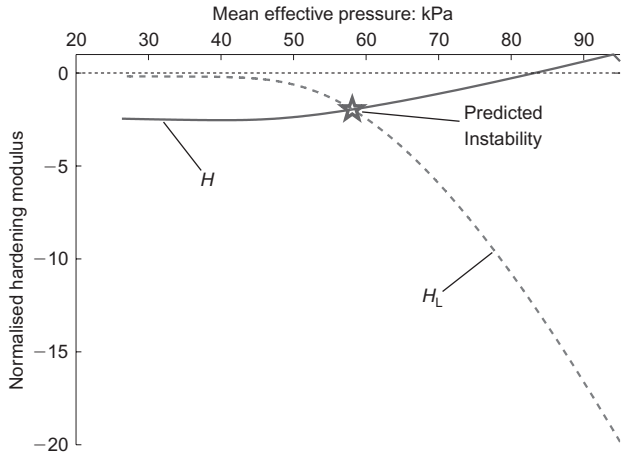

Fig. 5. Onset of liquefaction criterion for contractive sand at initial mean effective pressure of 100 kPa

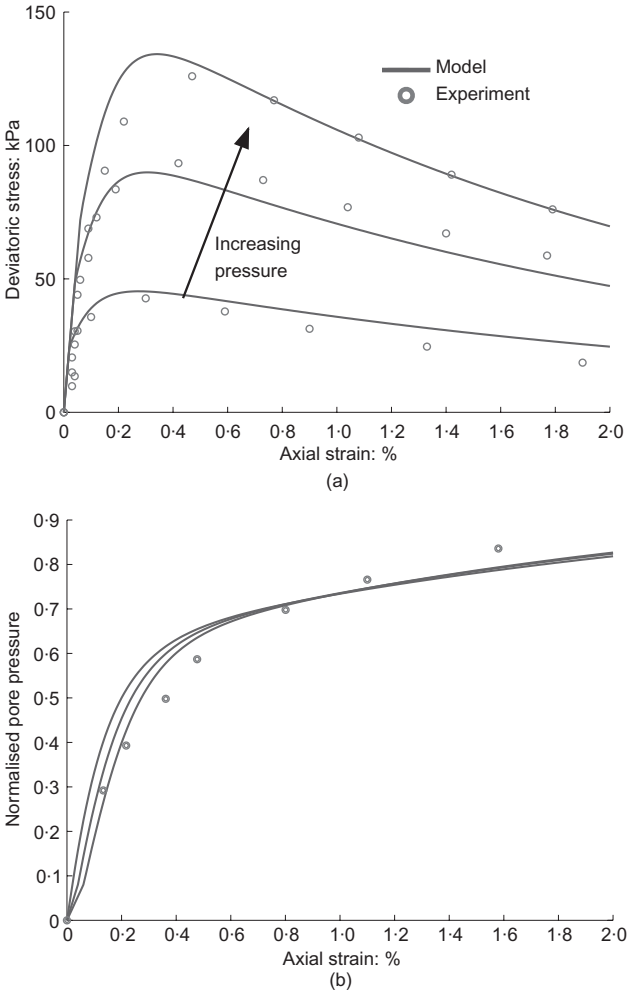

Fig. 6. Predicted (a) stress–strain curves and (b) normalised (by confining pressure) pore water pressures. Predicted results are compared with the experimental data by Doanh *et al.* (1997) from undrained triaxial compression at various confining pressures and constant void ratio

and 300 kPa consolidation pressure samples. The corresponding instability points are mapped in Fig. 4, where the predicted instability points are plotted. The instability points are then compared against the phenomenological flow liquefaction or instability line obtained experimentally by Doanh *et al.* (1997). It can be seen that the experimental instability and the predicted instabilities compare very favourably, with the predictions overpredicting the limiting stress ratio slightly (see Remark 2 below).

Experimentally, liquefaction instability was 'observed' in the experiments when there was a peak in the stress path followed by a sudden flow towards the critical state line (or failure line) (Doanh *et al.*, 1997). It is well known from other experimental results (Lade & Pradel, 1990) that the instability associated with liquefaction occurs at the peak of the stress path in a p'–q plot (see Fig. 1), and that such instability leads to the sudden collapse of the sample, which irreversibly flows towards failure. Liquefaction instability seems to be predicted correctly by the model in this case, since the onset of the instability is captured relatively accurately, and the instability is followed by a tendency of the samples to flow towards the CSL: that is, failure is ultimately attained. Furthermore, the predicted instability points suggest the existence of an instability line, which has also been observed experimentally by Lade & Pradel (1990), who applied Hill's criterion to explain the possibility of having an instability region well below the failure line. Indeed, it can be seen here that the proposed model is capable of detecting liquefaction instability, which is predicted to occur at the peaks of a p'–q plot and along a roughly straight line, delimiting the region of instability as observed experimentally.

The experimental and numerical results shown here display similar patterns: an initial increase in deviatoric stress, instability at peak, followed by large deformations and state culminating at the CSL. These patterns are clearly observable in Fig. 6, where the deviatoric stresses and pore pressures are plotted against axial strains. As expected, the samples with higher confining pressure display higher shear strengths. The peak strength in all samples was followed by pronounced strain-softening. Simultaneously, the pore water pressure builds up substantially, up to the onset of liquefaction instability. After the instability points the pore pressures steadily approach the corresponding confining pressure or a normalised value of unity. This asymptotic behaviour is synonymous with failure, and is preceded by the instability condition where the pore pressures range from 50% to 60% of the corresponding value of confining pressure. Hence using $p' \to 0$ as a condition for liquefaction instability is ambiguous, and should rather be regarded as liquefaction flow failure.

The predictions shown here are quite encouraging, since four distinct pieces of material behaviour are captured accurately

(*a*) the effective stress path
(*b*) the onset of liquefaction instability
(*c*) the stress–strain behaviour
(*d*) the pore water pressure build-up.

Simultaneous prediction of these features is not trivial, and showcases the promise of the proposed method realistically to capture the onset of liquefaction instability responsible for the ensuing material failure.

Remark 2. One interesting observation in light of the model adopted herein is to look at the limiting stress ratio when liquefaction occurred

$$\eta_L = M - \sqrt{\frac{-H_L}{\beta K}}(1 - N) \tag{23}$$

with $H_L \leqslant 0$, and where β is the non-associative parameter. The limiting stress ratio is not, however, a constant and hence cannot be interpreted as a material parameter. Rather, the limiting stress ratio is a function of the hardening modulus, which in turn is a function of the state. Hence, the limiting stress ratio is a necessary condition for liquefaction instability but not a sufficient condition and, as such, cannot be used to flag the onset of flow liquefaction, as typically done in practice.

Remark 3. As noted earlier, the material parameters used here are mostly obtained by 'fitting' the material response observed in one representative experiment. More rigorous experiments should be conducted truly to calibrate the model, say under-plane strain conditions, to then use the model in predicting behaviour, for the same sand, under triaxial compression, for instance.

Vaid & Chern (1983) experiments: constant consolidation pressure

The previous results help highlight the model's capability to predict the onset of liquefaction at a very loose state and under different consolidation pressures. In this section these results are complemented with a different set of experiments performed by Vaid & Chern (1983), where three samples of sand are loaded under undrained triaxial compression. The initial void ratio of each sample is different, to reflect different relative densities D_R. The sand used in the stress-controlled experiments is Ottawa sand, ASTM designation C-109. The maximum and minimum void ratios were 0·82 and 0·50 respectively. Vaid & Chern's intention was to investigate the effect of relative density on samples isotropically consolidated and subsequently sheared monotonically. Consequently, three samples with relative densities D_R of 37·8%, 45·9% and 48·2% were considered in the study. In the experimental programme, the first two samples with $D_R = 37{\cdot}8\%$ and $D_R = 45{\cdot}9\%$ were termed 'contractive', as they reached states of stress that led to loss of control, large deformations accompanied by large pore water pressures and subsequent failure. In contrast, the sample with $D_R = 48{\cdot}2\%$ was not as contractive, and did not develop a state of instability. It rather underwent a phase transformation and became 'dilative' so that pore water pressures decreased after such phase transformation. Fig. 3 shows the initial states and the loading paths followed in this set of experiments.

Similar to the previous results, the constitutive model is calibrated using the experimental result for the $D_R = 37{\cdot}8\%$ sample. Subsequently, the model parameters are held fixed, except for the void ratio, which is varied accordingly so as to use the same relative density as in the experiments. Also, because there is a higher relative density for each sample, the hardening parameter h is allowed to increase with the relative density. The model's predictions are qualitatively, and quantitatively, in agreement with the experiments. The material parameters used for the predictions are listed in Table 2.

Figure 7 shows the stress path obtained for the loosest sand with $D_R = 37{\cdot}8\%$. This response was used to obtain the material parameters for the constitutive model. Comparing the resulting stress path with the experimental one, it can be seen that the model underpredicts the response earlier in the loading programme and then tends to overpredict near failure. This is not too surprising, as the relative density

Table 2. Summary of material parameters for Vaid & Chern experiments dataset

Parameter	Value
Elastic compressibility, $\tilde{\kappa}$	0·0005
Shear modulus, μ: kPa	35 000
Plastic compressibility, $\tilde{\lambda}$	0·005
Critical state parameter, M	1·2
Reference specific volume, v_{c0}	1·688
Yield function, N	0·4
Plastic potential, $\bar{N}$	0·0
Hardening coefficient, h	30, 150, 550

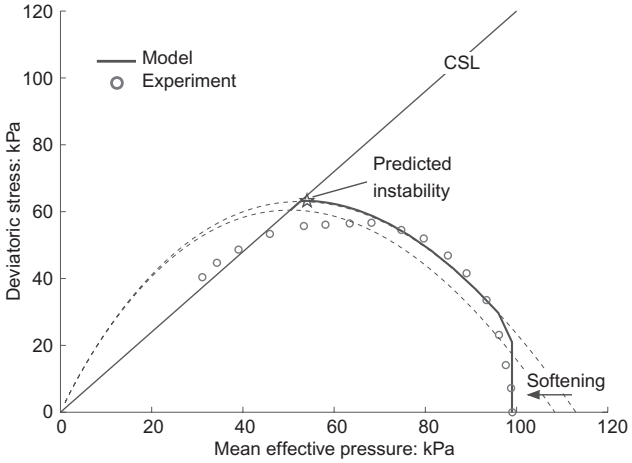

Fig. 7. Predicted stress path and onset of liquefaction instability for Ottawa sand at $D_R = 37{\cdot}8\%$

range in these experiments is quite tight. In this case, liquefaction is reported by Vaid & Chern, who call this sand contractive, and a sudden increase in pore pressures around the peak of the p'–q plot is reported. The model reproduces the behaviour by peaking and predicting that liquefaction instability will occur at the peak of the stress path. Incidentally, comparing this stress path with those obtained by Doanh *et al.*, the profound effect of elastic compressibility on the onset of liquefaction is noted. Recall that elastic incompressibility or $1/K \to 0$ forces any isotropic plasticity model to fail very close to zero dilation. This is indeed the case in this dataset, where failure occurs very close to the CSL. This is to be contrasted with the results obtained for the Doanh *et al.* experiments, where the elastic compressibility parameter $\tilde{\kappa} = 0{\cdot}002$ is an order of magnitude larger than that for the experiments performed by Vaid & Chern with $\tilde{\kappa} = 0{\cdot}0005$ (cf. Table 2). Additionally, Fig. 10 (see later) shows the stress and pore pressure evolution for the samples at various densities. It can be observed from this figure that the loosest sample contracts the most, leading to sustained softening and increased pore pressures.

The second sample analysed by Vaid & Chern had a relative density $D_R = 45{\cdot}9\%$, and therefore was expected to be a little less contractive than the first sample. Fig. 8 shows the stress path obtained experimentally for this sample. As before, the sample reached a peak in the stress path associated with a sudden increase in pore pressures and subsequent failure by monotonically flowing towards critical state. The experimental results are compared with the model predictions in this figure. This result is more predictive, as the material parameters in Table 2 are held fixed. Nevertheless, the material response predicted by the model is very close to that observed in the laboratory experiment. Furthermore, the model predicts liquefaction at the peak of the

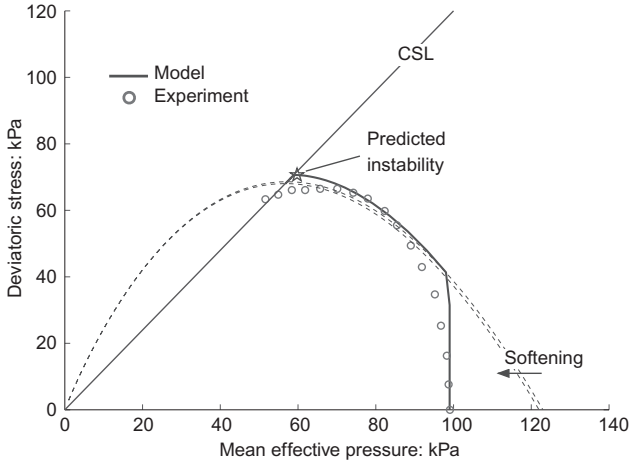

Fig. 8. Predicted stress path and onset of liquefaction instability for Ottawa sand at $D_R = 45{\cdot}9\%$

stress path, and shows monotonic flow towards the CSL. Instability occurs close to the critical state, as expected. Fig. 10 (see later) shows the stress and pore pressure evolution for the sample as a function of axial strain. Strain softening occurs in this sample, leading to an increase in pore pressure.

Finally, Vaid & Chern loaded a 'medium dense' sample of sand with $D_R = 48{\cdot}2\%$. This sample was not as contractant as the other two, and the signature behaviour of liquefaction was not observed. In fact, the stress path in Fig. 9 clearly shows an initially contractive behaviour, followed by a phase transformation, leading the sample to a rather dilative behaviour. This behaviour was not observed in the experiments performed by Doanh *et al.*, simply because the initial void ratios for all those experiments were kept constant and confinement pressure was sufficiently high. The phase transformation serves as a test for the liquefaction criterion and the constitutive model to be able to predict and differentiate between unstable behaviour and the phase transformation. The numerical predictions are plotted in Fig. 9, where very close agreement with the experimental data is observed. It is hard to see the phase transformation as the sample is too close to the CSL, but zooming into the data one can clearly spot the stress point where the transformation occurs. After this transformation, the sample tends to flow along the CSL in shear-hardening. Clearer phase transformations have been observed by, for example, decreasing the initial void ratio for Doanh *et al.* data. These results are encouraging, how-

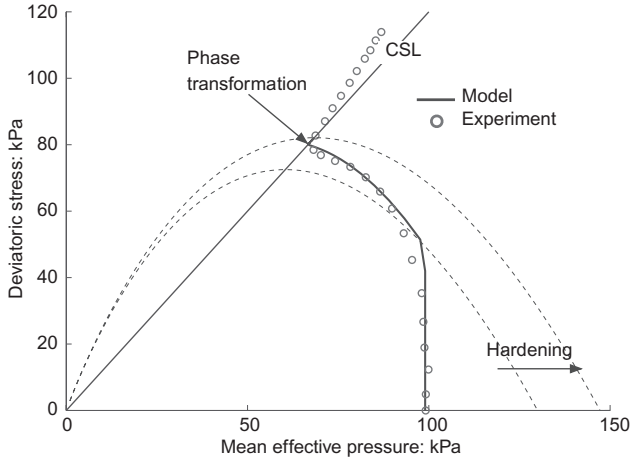

Fig. 9. Predicted stress path and onset of liquefaction instability for Ottawa sand at $D_R = 48{\cdot}2\%$

ever, as most of the stress path is accurately predicted by the model, and the model seems to be able to distinguish between liquefaction and no liquefaction for a very small difference in relative density.

As expected, the liquefaction condition does not flag instability in this case, even though the limiting stress ratio is reached. The limiting modulus H_L never intersects the hardening modulus H. Looking at the evolution of these moduli before the phase transformation, one would expect them to meet at some point. This is analogous to the results reported in the literature (Vaid & Chern, 1983; Yamamuro & Lade, 1997; Vaid & Sivathayalan, 2000), where the stress path, and even the pore pressures, seem to indicate that the sample is close to reaching the instability line, but instead a sudden phase transformation occurs (Ishihara *et al.*, 1975). One can observe the point where the phase transformation occurred, even in the evolution of the hardening modulus H. In fact, the stress path followed by the sample and the hardening modulus evolution show that phase transformations, in contrast to liquefaction instabilities, occur under material hardening. This can be further assessed by looking at Fig. 10, where hardening is observed for the densest sample and this is associated with a decrease in excess pore pressure.

Figure 10 shows the simulated stress–strain and excess pore pressure evolution curves for all three samples tested by Vaid & Chern. The contractive samples exhibit strain softening as a result of the liquefaction instability and the corresponding excess pore pressures steadily build up. In contrast, the dilative sample continuously hardens and the pore pressure decreases accordingly, with peak values below 60% of the confining pressure. The difference in the response is attributed to the initial state of the samples, which governs the dilatancy evolution, effectively controlling the pore pressure build-up.

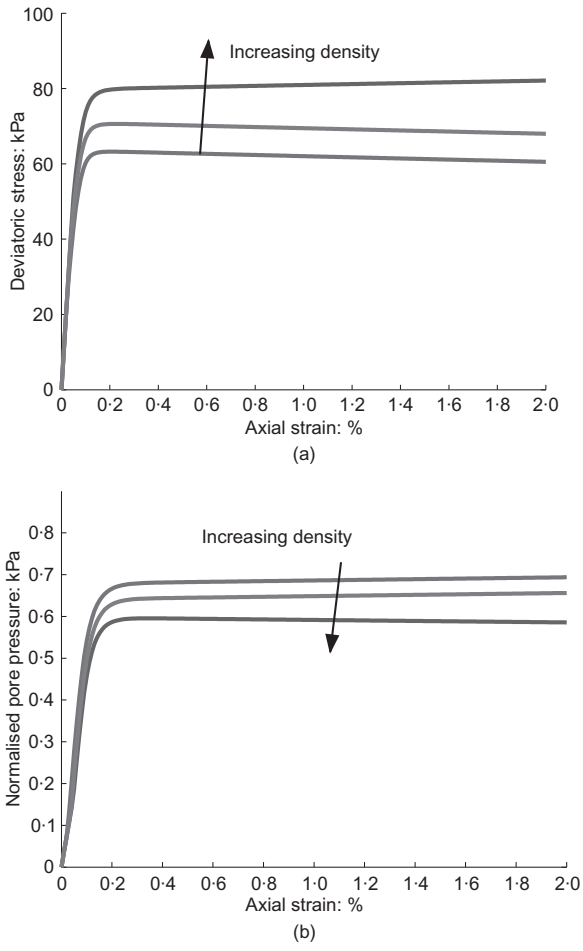

Fig. 10. Predicted (a) stress–strain curves and (b) normalised (by confining pressure) pore water pressures for the Vaid and Chern (1983) samples under undrained triaxial compression at various relative densities and constant confining pressure

CONCLUSION

A simple condition for liquefaction instability, applicable to all isotropic rate-independent elasto-plastic models, has been presented. Furthermore, the instability has been shown to emanate from forcing an undrained or isochoric bifurcation, which would lead to liquefaction conditions, rather than shear localisation. However, the framework for either instability is the same, and only one model has been used to predict both, based solely on the state of the granular media and the kinematics imposed (e.g. drained or undrained conditions, plane strain or biaxial loading). A model to simulate the behaviour of sands under dense and loose conditions has been presented and used to perform predictions for the onset of liquefaction instability. The instability framework was then used in a predictive exercise and compared against experimental results obtained a few decades ago by two different research groups. The results are encouraging, as they show that the proposed model is capable of reproducing behaviour obtained from undrained triaxial compression testing of sands at different confinement pressures and relative densities. Furthermore, the model captures phase transformations, and does not detect liquefaction instability in those situations. The instability line is clearly obtained and closely aligned to that obtained from experiments. Liquefaction instability is predicted as a function of the state, rather than a material property. The present results are encouraging and seem to open the door to better understanding, modelling, prediction and capture of catastrophic instabilities in saturated granular materials.

ACKNOWLEDGEMENTS

The author is very grateful to the anonymous reviewers for their insightful comments. Their expert opinion helped to improve the paper substantially. This research was partially funded by the U.S. National Science Foundation under grant number CMMI-0726908. This support is gratefully acknowledged.

NOTATION

$\boldsymbol{c}^{\mathrm{ep}}$	canonical elastoplastic tangent
D	dilatancy
D^*	limiting dilatancy
D_R	relative density
F	yield function
$\boldsymbol{g}$	gravity vector
$\dot{\boldsymbol{\varepsilon}}$	total strain rate
$\dot{\boldsymbol{\varepsilon}}^e$	elastic strain rate
$\dot{\boldsymbol{\varepsilon}}^p$	plastic strain rate
$\dot{\varepsilon}_v$	volumetric strain rate invariant
$\dot{\varepsilon}_s$	deviatoric strain invariant
$\dot{\varepsilon}_v^p$	plastic volumetric strain rate invariant
$\dot{\varepsilon}_s^p$	plastic deviatoric strain rate invariant
H_L	limiting hardening module
H	hardening madulus
K	elastic bulk modulus of sand
h	hardening coefficient
$\tilde{\kappa}$	elastic compressibility of sand
$\boldsymbol{L}$	Borja's liquefaction matrix
$\mathbf{1}$	identity matrix
M	critical state parameter
N	shape parameter for yield surface

$\overline{N}$	shape parameter for plastic potential surface
p	pore water pressure
p'	effective mean normal stress invariant
Q	plastic potential function
q	deviatoric stress invariant
$\boldsymbol{q}$	relative (Darcy) flow vector
$\boldsymbol{v}$	velocity of solid
β	non-associativity parameter
η_L	limiting effective stress ratio
η	stress ratio
$\boldsymbol{\lambda}$	plastic compressibility of sand
μ	elastic shear modulus of sand
π_{i}	image pressure or size parameter for yield surface
π_{i}^*	limiting image pressure
$\overline{\pi}_{\mathrm{i}}$	size parameter for plastic potential
ρ	density of mixture
$\boldsymbol{\sigma}$	total stress tensor
$\boldsymbol{\sigma}'$	effective stress tensor
$\boldsymbol{\xi}'$	deviatoric stress tensor
v	specific volume
v_{c0}	reference specific volume
ψ	state parameter
ψ_{i}	image state parameter

REFERENCES

Anandarajah, A. (1994). Procedures for elasto-plastic liquefaction modeling of sands. *J. Engng Mech.* **120**, No. 7, 1563–1587.

Andrade, J. E. & Borja, R. I. (2006). Capturing strain localization in dense sands with random density. *Int. J. Numer. Methods Engng* **67**, No. 11, 1531–1564.

Andrade, J. E. & Borja, R. I. (2007). Modeling deformation banding in dense and loose fluid-saturated sands. *Finite Elements Anal. Des.* **43**, No. 5, 361–383.

Andrade, J. E. & Ellison, K. C. (2008). Evaluation of a predictive constitutive model for sands. *J. Geotech. Geoenviron. Engng* **134**, No. 12, 1825–1828.

Andrade, J. E., Baker, J. W. & Ellison, K. C. (2008). Random porosity fields and their influence on the stability of granular media. *Int. J. Numer. Anal. Methods Geomech.* **32**, No. 19, 1147–1172.

Atkin, R. J. & Craine, R. E. (1976). Continuum theories of mixture: basic theory and historical development. *Q. J. Mech. Appl. Math.* **29**, No. 5, 209–244.

Been, K. and Jeffries, M. (2004). Stress-dilatancy in very loose sand. *Can. Geotech. J.* **41**, 972–989.

Bishop, A. W. (1973). The stability of tips and spoil heaps. *Q. J. Engng Geol.* **6**, 335–376.

Borja, R. I. (2002). Bifurcation of elastoplastic solids to shear band mode at finite strains. *Comput. Methods Appl. Mech. Engng* **191**, No. 46, 5287–5314.

Borja, R. I. (2006). Condition for liquefaction instability in fluid-saturated granular soils. *Acta Geotech.* **1**, No. 4, 211–224, 2006.

Borja, R. I. & Andrade, J. E. (2006). Critical state plasticity, Part VI: Meso-scale finite element simulation of strain localization in discrete granular materials. *Comput. Methods Appl. Mech. Engng* **195**, Nos 37–40, 5115–5140.

Borja, R. I. & Tamagnini, C. (1998). Cam-Clay plasticity, Part III: Extension of the infinitesimal model to include finite strains. *Comput. Methods Appl. Mech. Engng* **155**, Nos 1–2, 73–95.

Borja, R. I., Tamagnini, C. & Amorosi, A. (1997). Coupling plasticity and energy-conserving elasticity models for clays. *J. Geotech. Geoenviron. Engng ASCE* **123**, No. 10, 948–957.

Bowen, R. M. (1976). Theory of mixtures. In *Continuum physics* (ed. A. C. Eringen), Vol. 3: *Mixtures and EM field theories*, pp. 1–127. New York: Academic Press.

Castro, G. (1969). *Liquefaction of sands*, Harvard Soil Mechanics Series 81. Cambridge, MA: Harvard University.

Doanh, T., Ibraim, E. & Matiotti, R. (1997). Undrained instability of very loose Hostun sand in triaxial compression and extension. Part 1: Experimental observations. *Mech. Cohesive-Frictional Mater.* **2**, No. 1, 47–70.

Dubujet, Ph. & Doanh, T. (1997). Undrained instability of very loose Hostun sand in triaxial compression and extension. Part 2: Theoretical analysis using an elastoplasticity model. *Mech. Cohesive-Frictional Mater.* **2**, No. 1, 71–92.

Hill, R. (1958). A general theory of uniqueness and stability in elastic-plastic solids. *J. Mech. Phys. Solids* **6**, No. 3, 236–249.

Houlsby, G. T. (1985). The use of a variable shear modulus in elasto-plastic models for clays. *Comput. Geotech.* **1**, No. 1, 3–13.

Imposimato, S. & Nova, R. (1998a). An investigation on the uniqueness of the incremental response of elastoplastic models for virgin sand. *Mech. Cohesive-Frictional Mater.* **3**, No. 1, 65–87.

Imposimato, S. & Nova, R. (1998b). Instability of loose sand specimens in undrained tests. In *Localization and bifurcation theory for soils and rocks* (eds T. Adachi, F. Oka and A. Yashima), pp. 313–322. Rotterdam: Balkema.

Ishihara, K., Tatsuoka, F. & Yasuda, S. (1975). Undrained deformation and liquefaction of sand under cyclic stresses. *Soils Found.* **15**, No. 1, 29–44.

Jefferies, M. G. (1993). Nor-Sand: a simple critical state model for sand. *Géotechnique* **43**, No. 1, 91–103.

Kramer, M. G. (1996). *Geotechnical earthquake engineering*. Upper Saddle River, NJ: Prentice Hall.

Lade, P. V. (1992). Static instability and liquefaction of loose fine sandy slopes. *J. Geotech. Engng ASCE* **118**, No. 1, 51–71, 1992.

Lade, P. V. (1999). Instability of granular materials. In *Physics and mechanics of soil liquefaction* (eds P. V. Lade and J. A. Yamamuro), pp. 3–16. Rotterdam: Balkema.

Lade, P. V. & Pradel, D. (1990). Instability and plastic flow of soils. I: Experimental observations. *J. Engng Mech.* **116**, No. 11, 2532–2550.

Manzari, M. T. & Dafalias, Y. F. (1997). A critical state two-surface plasticity model for sands. *Géotechnique* **43**, No. 2, 255–272.

Marsden, J. E. & Hughes, T. J. R. (1983). *Mathematical theory of elasticity.* Englewood Cliffs, NJ: Prentice Hall.

Mroz, Z., Boukpeti, N. & Drescher, A. (2003). Constitutive model for static liquefaction. *Int. J. Geomech.* **3**, No. 3, 133–144.

National Research Council (1985). *Liquefaction of soils during earthquakes*. Washington, DC: National Academy Press.

Nova, R. (1994). Controllability of the incremental response of soil specimens subjected to arbitrary loading programmes. *J. Mech. Behavior Mater.* **5**, No. 2, 193–201.

Pradel, D. & Lade, P. V. (1990). Instability and plastic flow of soils. II: Analytical investigation. *J. Engng Mech.* **116**, No. 1, 2551–2566.

Roscoe, K. H. & Burland, J. H. (1968). On the generalized stress–strain behavior of 'wet' clay. In *Engineering plasticity* (eds J. Heyman and F. A. Leckie), pp. 535–609. Cambridge: Cambridge University Press.

Rudnicki, J. W. & Rice, J. R. (1975). Conditions for localization of deformation in pressure-sensitive dilatant materials. *J. Mech. Phys. Solids* **23**, No. 6, 371–394.

Schofield, A. & Wroth, P. (1968). *Critical state soil mechanics*. New York: McGraw-Hill.

Seed, H. B., Idriss, I. M., Lee, K. L. & Makdisi, F. I. (1971). Dynamic analysis of the slide in the Lower San Fernando dam during the earthquake of February 9, 1971. *J. Geotech. Engng Div. ASCE* **101**, No. 9, 889–911.

Vaid, Y. P. & Chern, J. C. (1983). Effect of static shear on resistance to liquefaction. *Soils Found.* **23**, No. 1, 47–60.

Vaid, Y. P. & Sivathayalan, S. (2000). Fundamental factors affecting liquefaction susceptibility of sands. *Can. Geotech. J.* **37**, No. 3, 592–606.

Wang, Z.-L., Dafalias, Y. F., Li, X.-S. & Makdisi, F. I. (2002). State pressure index for modeling sand behavior. *J. Geotech. Geoenviron. Engng* **128**, No. 6, 511–519, 2002.

Yamamuro, J. A. & Lade, P. V. (1997). Static liquefaction of very loose sands. *Can. Geotech. J.* **34**, No. 6, 905–917.